

PROCEEDINGS OF SPIE

SPIEDigitalLibrary.org/conference-proceedings-of-spie

Open-source Gauss-Newton-based methods for refraction-corrected ultrasound computed tomography

Ali, Rehman, Hsieh, Scott, Dahl, Jeremy

Rehman Ali, Scott Hsieh, Jeremy Dahl, "Open-source Gauss-Newton-based methods for refraction-corrected ultrasound computed tomography," Proc. SPIE 10955, Medical Imaging 2019: Ultrasonic Imaging and Tomography, 1095508 (15 March 2019); doi: 10.1117/12.2511319

SPIE.

Event: SPIE Medical Imaging, 2019, San Diego, California, United States

Open-Source Gauss-Newton-Based Methods for Refraction-Corrected Ultrasound Computed Tomography

Rehman Ali^a, Scott Hsieh^b, and Jeremy Dahl^c

^aDepartment of Electrical Engineering, Stanford University, Palo Alto, CA, 94305 USA

^bDepartment of Radiology, University of California Los Angeles, Los Angeles, CA, 90095 USA

^cDepartment of Radiology, Stanford School of Medicine, Palo Alto, CA, 94304 USA

ABSTRACT

This work presents refraction-corrected sound speed reconstruction techniques for transmission-based ultrasound computed tomography using a circular transducer array. Pulse travel times between element pairs can be calculated from slowness (the reciprocal of sound speed) using the eikonal equation. Slowness reconstruction is posed as a nonlinear least squares problem where the objective is to minimize the error between measured and forward-modeled pulse travel times. The Gauss-Newton method is used to convert this problem into a sequence of linear least-squares problems, each of which can be efficiently solved using conjugate gradients. However, the sparsity of ray-pixel intersection leads to ill-conditioned linear systems and hinders stable convergence of the reconstruction. This work considers three approaches for resolving the ill-conditioning in this sequence of linear inverse problems: 1) Laplacian regularization, 2) Bayesian formulation, and 3) resolution-filling gradients. The goal of this work is to provide an open-source example and implementation of the algorithms used to perform sound speed reconstruction, which is currently being maintained on Github: <https://github.com/rehmanali1994/refractionCorrectedUSCT.github.io>

Keywords: Nonlinear inverse problems, Gauss-Newton method, regularization, Bayesian, resolution-filling

1. INTRODUCTION

The goal of ultrasound computed tomography (USCT) is to measure the material properties of human tissue, such as sound speed and attenuation, with a high degree of accuracy and spatial resolution. Most applications of USCT have been in breast imaging, especially breast cancer screening, because of the relative ease of obtaining and recording the ballistic-wave transmission through the breast.^{1–6} In this context, sound speed and attenuation have been used as sources of image contrast. Furthermore, sound speed and attenuation maps have been used to construct refraction- and attenuation-corrected maps of tissue echogenicity with high accuracy and spatial resolution based on the angular compounding of images produced by the backscattered echoes.^{7,8} USCT has also been widely used for refraction and attenuation correction in photoacoustic imaging in a manner analogous to how X-ray computed tomography (CT) has been used for attenuation correction in positron emission tomography (PET).^{9,10}

This report specifically investigates USCT for sound speed estimation in inhomogeneous sound-speed media. Techniques for sound speed estimation strategies generally fall into two broad categories: full-waveform inversion (FWI),^{11,12} and refracted ray-path models.^{13,14} FWI is generally regarded as the most accurate approach for USCT reconstruction because it uses repeated simulations of the wave equation to iteratively estimate the parameters responsible for reproducing the observed channel data most closely. Because FWI involves directly matching the results of the wave equation to observed channel data, FWI should take both refraction and diffraction into account in the reconstruction. However, FWI is highly computationally intensive. Because of a substantially lower computation time, the refracted ray models tend to be preferred over FWI.^{13–15} Furthermore, refracted-ray path reconstructions can be used as initial conditions for FWI to improve their convergence. However, their key drawback is the inability to account for diffraction, which leads to poorer resolution in the reconstructed image.

Further author information: (Send correspondence to Rehman Ali)

Rehman Ali: E-mail: rali8@stanford.edu

In general, computed tomography (CT) attempts to reconstruct the image of an object from its projections. For example, in X-ray CT, the measured attenuation of each X-ray beam is effectively a line-integral projection of the attenuation distribution encountered along the path of the X-ray beam.¹⁶ After sufficiently sampling different integration paths, it is possible to carefully invert a linear system of line integrals to reconstruct the attenuation distribution.^{17,18}

In a similar manner, travel time-based (as opposed to FWI-based) USCT measures the travel times of sound waves transmitted through human tissue in order to reconstruct a sound speed distribution.¹ The travel time of sound through human tissue can be understood as a line-integral of slowness (defined as reciprocal of sound speed) over the path that the sound traveled. However, a key difference between X-ray CT and USCT is that whereas the path of an X-ray beam is often a straight line from source to detector, the path of sound is dependent on the underlying sound speed distribution between source and detector¹³ because a wave always follows a refracted path that minimizes the travel time between two points.^{19,20} Standard CT reconstruction, such as filtered backprojection (FBP), fails to take refraction into account because it makes a straight ray-path assumption (Figure 1) resulting in poor resolution.

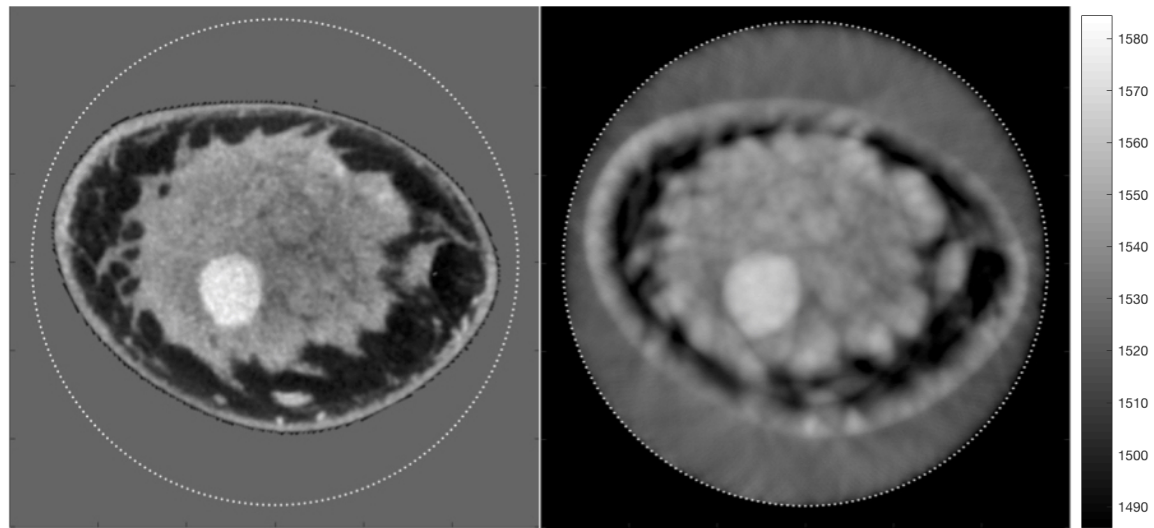


Figure 1. True Sound Speed [m/s] (Left) and Standard FBP Reconstruction (Right) for a 256-Element Ring Array Surrounding an Inhomogeneous Medium. This sound speed map was adapted and modified from a contrast-enhanced cone-beam breast CT image in work from the Diagnostic Breast Center Göttingen (<https://doi.org/10.1016/j.tranon.2017.08.010>)²¹ under the Creative Commons Attribution-NonCommercial-No Derivatives License (CC BY NC ND) (<https://creativecommons.org/licenses/by-nc-nd/4.0/>)

Previous methods for refraction-corrected USCT have used nonlinear optimization to minimize model misfit of measured travel times and a regularization term to enforce continuity of the slowness reconstruction.^{13,14} Nonlinear programming strategies can be time consuming because they require multiple gradient and objective evaluations, each of which performs several evaluations of the eikonal equation and ray-tracing procedures, to reach the optimum.¹³ We propose to use the Gauss-Newton method for solving the nonlinear optimization problem by solving a sequence of linear least-squares problems, each of which is efficiently solved using conjugate gradients.^{22,23} The Gauss-Newton method reduces the total number of eikonal equation evaluations and ray-tracing procedures by performing a single set of these operations just prior to solving each linear least-squares problem.

However, as shown in prior work,¹³ the sparsity of ray-pixel intersection leads to ill-conditioning of the linear system at each step of the Gauss-Newton method. Enforcement of spatial continuity and smoothness of the slowness reconstruction can overcome this ill-conditioning problem. In this work we consider three different methods for enforcing this spatial continuity. The first method is Laplacian regularization, which enforces image smoothness by penalizing the spatial Laplacian of the reconstructed image. The second method involves a

Bayesian reformulation where observed data is used in conjunction with a prior mean and covariance over all pixels in the image. In this case, image smoothness becomes enforced by the covariance structure of the prior. The final method requires no regularization or problem reformulation; instead, the gradients used in CG are blurred using a kernel with decreasing radius in order to stabilize the reconstruction and resolve smaller details with each iteration. This blurring effectively restricts the solution of the original linear least-squares problems to smooth images.

Although techniques for travel time USCT on a circular transducer array have been well explored,^{1,13,14} there is a lack of openly available codes that perform refraction-corrected, or bent-ray, USCT reconstruction.^{24,25} We aim to provide an open-source implementation of refraction-corrected travel-time USCT for each of the three algorithms mentioned above.

2. BACKGROUND

2.1 Eikonal Equation and Ray Tracing

The travel time $T(x, y)$ of an acoustic wave from a source location (x_{src}, y_{src}) to every location in space (x, y) is described by the two-dimensional eikonal equation,

$$\sqrt{\left(\frac{\partial T}{\partial x}\right)^2 + \left(\frac{\partial T}{\partial y}\right)^2} = s(x, y), \quad (1)$$

subject to the boundary condition $T(x_{src}, y_{src}) = 0$, where $s(x, y)$ is the slowness, or reciprocal of sound speed, at position (x, y) . The fast marching method (FMM) is used to solve the eikonal equation for $T(x, y)$ given $s(x, y)$ and (x_{src}, y_{src}) .^{19,20,26,27} The spatial gradient of the resulting travel time function $\nabla T(x, y) = \begin{bmatrix} \frac{\partial T}{\partial x} & \frac{\partial T}{\partial y} \end{bmatrix}$ is used to trace the refracted ray path from a receiver location (x_{rx}, y_{rx}) to the source location (x_{src}, y_{src}) . Example ray tracings from individual elements on the ring array and media from Fig. 1 are shown in Fig. 2.

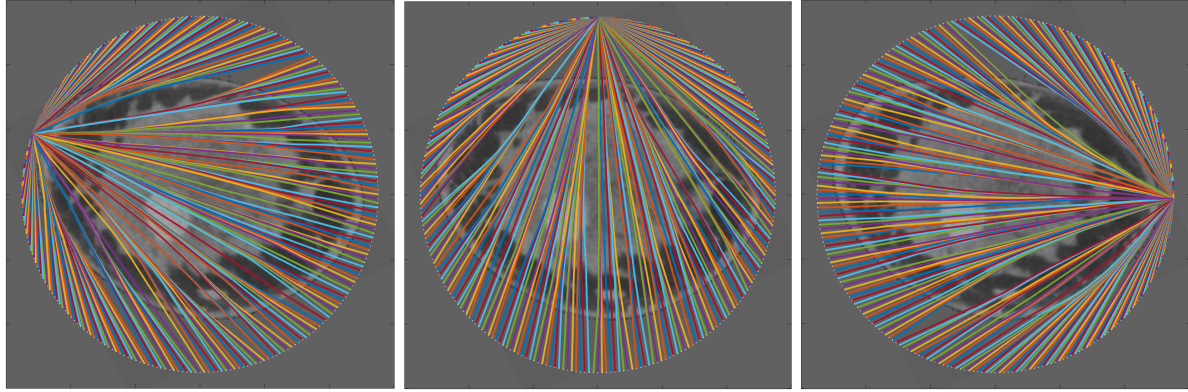


Figure 2. Ray Tracing from Different Source Elements on Ring Array through the Inhomogeneous Medium in Fig. 1. Rays tend to avoid low sound speed (or high slowness) regions because waves travel the path that minimizes the travel time between any two points.

2.2 Reconstruction Problem

The goal of refraction-corrected USCT reconstruction is to find the slowness distribution $s(x, y)$ that best explains the observed pulse travel times measured between each pair of transmit and receive elements on the circular transducer array. This can be restated as a least-squares minimization problem,

$$\underset{z}{\text{minimize}} \quad E(z) = \|t(z) - t_{obs}\|_2^2, \quad (2)$$

where $z \in \mathbb{R}_+^n$ is the vector of pixel values in the slowness distribution $s(x, y)$, $t(z) \in \mathbb{R}_+^m$ is the vector of pulse travel times between each pair of transmit and receive elements for this slowness distribution, and $t_{obs} \in \mathbb{R}_+^m$ is the vector of observed pulse travel times between the same transmit and receive element pairings.

The gradient of the objective of (2) with respect to z is $2J(z)^T(t(z) - t_{obs})$, where $J(z) \in \mathbb{R}_+^{m \times n}$ is the Jacobian of $t(z)$. The Jacobian $J(z)$ is a matrix representation of the line integrals that have to be performed over the slowness distribution z to obtain the travel times between each source-receiver pair. In order to calculate $J(z)$, the refracted ray paths between each source-and-receiver pair over the slowness distribution specified by z must first be determined using the FMM and ray tracing procedure as described in the previous section (2.1). The entries of $J(z)$ are the path length of each ray (rows of $J(z)$) over each pixel of z (columns of $J(z)$), which implies that $t(z) = J(z)z$.^{13,14} Thus, the refraction-corrected USCT reconstruction problem can be expressed as

$$\underset{z}{\text{minimize}} \quad E(z) = \|J(z)z - t_{obs}\|_2^2, \quad (3)$$

2.3 Gauss-Newton Method

The Gauss-Newton method solves the original nonlinear least-squares reconstruction problem in (3) as a sequence of linear-least squares approximations,

$$\underset{z_{i+1}}{\text{minimize}} \quad \hat{E}(z_{i+1}) = \|J(z_i)z_{i+1} - t_{obs}\|_2^2, \quad (4)$$

where $z_i \in \mathbb{R}_+^n$ is the optimized slowness distribution from the previous iteration i of the Gauss-Newton method, and $z_{i+1} \in \mathbb{R}_+^n$ is the slowness distribution being optimized in the current iteration $i + 1$ of the Gauss-Newton method. The gradient of the objective (4) for this problem is

$$\nabla \hat{E}(z_{i+1}) = 2J(z_i)^T(J(z_i)z_{i+1} - t_{obs}), \quad (5)$$

Although it appears that the objective can best be optimized using this gradient, the ray paths encoded by the Jacobian $J(z_i)$ do not touch every pixel in the slowness distribution z_i . As a result, this gradient definition results in a highly non-smooth and non-physical reconstruction of the slowness. We consider three different strategies for enforcing the smoothness of the slowness reconstruction: Laplacian regularization (2.3.1), Bayesian reformulation (2.3.2), and resolution-filling gradients (2.3.3). The Gauss-Newton method employed throughout this paper follows the template given in Algorithm 1. The GAUSSNEWTONUPDATE subroutine in Algorithm 1 depends on the strategy used to enforce smoothness of the slowness reconstruction.

Algorithm 1 Gauss-Newton Slowness Reconstruction Algorithms

```

1: Initialize  $z_0$  to a uniform distribution:  $z_0 = s_{init}\mathbf{1}$                                  $\triangleright s_{init} = \frac{1}{1540\frac{m}{s}}$ 
2: for  $n = 1, \dots, N$  do                                                  $\triangleright N$  Iterations of Gauss-Newton
3:   Use FMM and ray-tracing to calculate  $H = J(z_{n-1})$ 
4:    $z_n = \text{GAUSSNEWTONUPDATE}(z_{n-1}, H, t_{obs}, \dots \text{other parameters})$ 
5: end for
6: return  $z_N$ 

```

2.3.1 Laplacian Regularization

Given a matrix approximation $L \in \mathbb{R}^{n \times n}$ of the Laplacian operator ∇^2 , the matrix-vector product Lz can be interpreted as the vector of pixels values for the Laplacian of the slowness distribution $\nabla^2 s(x, y)$. The objective in (3) can be augmented by adding a regularization term (with regularization parameter $\alpha \in \mathbb{R}_+$) that penalizes the Laplacian of the reconstructed slowness image. This yields

$$\underset{z}{\text{minimize}} \quad E(z) = \|J(z)z - t_{obs}\|_2^2 + \alpha^2\|Lz\|_2^2. \quad (6)$$

Because the Laplacian can be used as a measure of image roughness, this Laplacian regularization essentially penalizes image roughness and promotes the smoothness of the final slowness reconstruction. The corresponding linearized least-squares objective for the Gauss-Newton method is

$$\underset{z_{i+1}}{\text{minimize}} \quad \hat{E}(z_{i+1}) = \|J(z_i)z_{i+1} - t_{obs}\|_2^2 + \alpha^2\|Lz_{i+1}\|_2^2 = \left\| \begin{bmatrix} J(z_i) \\ \alpha L \end{bmatrix} z_{i+1} - \begin{bmatrix} t_{obs} \\ 0 \end{bmatrix} \right\|_2^2. \quad (7)$$

The conjugate gradient (CG) algorithm²² can be used to optimize the regularized least-squares objective given in (7); the corresponding implementation is given by the GAUSSNEWTONUPDATE in Algorithm 2.

Algorithm 2 Gauss-Newton Update with Laplacian Regularization

```

1: procedure GAUSSNEWTONUPDATE( $z_{n-1}, H, t_{obs}, \alpha, L$ )
2:    $G = \begin{bmatrix} H \\ \alpha L \end{bmatrix}$ ,  $d = \begin{bmatrix} t_{obs} \\ 0 \end{bmatrix}$ ,  $m_0 = z_{n-1}$ ,  $p_{-1} = 0$ ,  $\beta_{-1} = 0$ ,
3:    $s_0 = Gm_0 - d$ , and  $r_0 = G^T s_0$ 
4:   for  $k = 0, \dots, K-1$  do ▷  $K$  Iterations of Conjugate Gradient
5:      $p_k = -r_k + \beta_{k-1}p_{k-1}$ 
6:      $\alpha_k = \|r_k\|_2^2/\|Gp_k\|_2^2$ 
7:      $m_{k+1} = m_k + \alpha_k p_k$ 
8:      $s_{k+1} = s_k + \alpha_k Gp_k$ 
9:      $r_{k+1} = G^T s_{k+1}$ 
10:     $\beta = \|r_{k+1}\|_2^2/\|r_k\|_2^2$ 
11:   end for
12:   return  $m_K$ 
13: end procedure

```

2.3.2 Bayesian Reformulation

Linearization of $t(z) = t_{obs}$ with additive noise results in the following observation equation

$$t_{obs} = Hz + v, \quad (8)$$

where $H \in \mathbb{R}_+^{m \times n}$ is a linearization of $t(z)$ around some slowness distribution z , and $v \in \mathbb{R}_+^n$ is a Gaussian random vector with mean 0 and covariance matrix $R \in \mathbb{R}_+^{n \times n}$. The likelihood function can then be written as the probability density function for t_{obs} given z

$$f(t_{obs}|z) = (2\pi)^{-\frac{n}{2}} (\det R)^{-\frac{1}{2}} \exp \left[-\frac{1}{2} (t_{obs} - Hz)^T R^{-1} (t_{obs} - Hz) \right]. \quad (9)$$

The Gaussian prior distribution on z with mean $z_{prior} \in \mathbb{R}_+^n$ and covariance $Q \in \mathbb{R}_+^{m \times m}$ can be written as

$$f'(z) = (2\pi)^{-\frac{m}{2}} (\det Q)^{-\frac{1}{2}} \exp \left[-\frac{1}{2} (z - z_{prior})^T Q^{-1} (z - z_{prior}) \right]. \quad (10)$$

The posterior distribution on z can be written as

$$f''(z) = f(t_{obs}|z)f'(z) \propto \exp \left[-\frac{1}{2} (t_{obs} - Hz)^T R^{-1} (t_{obs} - Hz) - \frac{1}{2} (z - z_{prior})^T Q^{-1} (z - z_{prior}) \right]. \quad (11)$$

Minimizing the negative log of $f''(z)$ results in the least-squares objective

$$\underset{z}{\text{minimize}} \quad E_{\text{Bayesian}}(z) = \frac{1}{2} (t_{obs} - Hz)^T R^{-1} (t_{obs} - Hz) + \frac{1}{2} (z - z_{prior})^T Q^{-1} (z - z_{prior}). \quad (12)$$

A closed form solution to this optimization problem is

$$\begin{aligned} z &= z_{prior} + (Q^{-1} + H^T R^{-1} H)^{-1} H^T R^{-1} (t_{obs} - H z_{prior}) \\ &= z_{prior} + Q H^T (H Q H^T + R)^{-1} (t_{obs} - H z_{prior}). \end{aligned} \quad (13)$$

This closed-form Bayesian solution is reminiscent of the Kalman filter^{28,29} where $t_{obs} - H z_{prior}$ is the innovation and $Q H^T (H Q H^T + R)^{-1}$ is the Kalman gain for the innovation. This solution can be broken into two parts,

$$(H Q H^T + R) \xi = t_{obs} - H z_{prior}, \quad (14)$$

$$z = z_{prior} + Q H^T \xi. \quad (15)$$

The solution $\xi \in \mathbb{R}^n$ of equation (14) is inserted into equation (15), which yields the Bayesian reconstruction of the slowness image. The covariance matrix R over the observed travel times is assumed to be a scaled version of the identity matrix so that $R = \alpha I$ where $\alpha \in \mathbb{R}$. If the covariance structure of the pixels in the slowness image is assumed to be spatially invariant, the covariance matrix Q can be understood as a convolution operator whose kernel represents the covariance of each pixel with the pixels surrounding it. This work uses a Gaussian blur for the convolution operator. Furthermore, H is a sparse matrix in this work. Equation (14) can be solved for ξ using conjugate gradient^{22,23} because $H Q H^T + R$ is symmetric and positive semidefinite. Furthermore, conjugate gradient does not explicitly require construction and storage of $H Q H^T + R$ as long as the matrix-vector multiplication $(H Q H^T + R)v$ can be calculated for any $v \in \mathbb{R}^n$. The implementation of equation (15) using the conjugate gradient solution of equation (14) is given by the GAUSSNEWTONUPDATE in Algorithm 3.

Algorithm 3 Gauss-Newton Update using Bayesian Framework

```

1: procedure GAUSSNEWTONUPDATE( $z_{n-1}, H, t_{obs}, \alpha, Q$ )
2:   procedure A( $x$ )
3:     return  $H(Q(H^T x)) + \alpha x$ 
4:   end procedure
5:    $x_0 = z_{n-1}$ ,  $b = t_{obs} - Hx_0$ ,
6:    $p_{-1} = 0$ ,  $\beta_{-1} = 0$ ,  $r_0 = A(x_0) - b$ 
7:   for  $k = 0, \dots, K - 1$  do ▷  $K$  Iterations of Conjugate Gradient
8:      $p_k = -r_k + \beta_{k-1} p_{k-1}$ 
9:      $\alpha_k = \|r_k\|_2^2 / (p_k^T A(p_k))$ 
10:     $x_{k+1} = x_k + \alpha_k p_k$ 
11:     $r_{k+1} = r_k + \alpha_k A(p_k)$ 
12:     $\beta = \|r_{k+1}\|_2^2 / \|r_k\|_2^2$ 
13:   end for
14:   return  $x_K$ 
15: end procedure

```

2.3.3 Resolution-Filling Gradients

One way to address the ill-conditioning in (3) is to blur the gradient image (5) by $B_k \in \mathbb{R}_+^{n \times n}$, which describes a 2D convolution with a Gaussian blurring kernel. Here the subscript k denotes the k th iteration of the CG algorithm used to optimize the i th iteration of the Gauss-Newton method. The blurring radius of the blurring kernel is gradually decreased with each iteration k in order to progressively resolve smaller details in the slowness distribution, hence the name resolution-filling gradients. Overall this resolution-filling gradient is

$$\nabla \hat{E}(z_{i+1}) = 2B_k J(z_i)^T (J(z_i)z_{i+1} - t_{obs}). \quad (16)$$

Algorithm 4 provides the definition of GAUSSNEWTONUPDATE for the resolution-filling CG algorithm.

Algorithm 4 Gauss-Newton Update using Resolution-Filling Gradients

```
1: procedure GAUSSNEWTONUPDATE( $z_{n-1}, H, t_{obs}, B_0, \dots, B_{K-1}$ )
2:    $G = H, d = t_{obs}, m_0 = z_{n-1}, p_{-1} = 0, \beta_{-1} = 0,$ 
3:    $s_0 = Gm_0 - d$ , and  $r_0 = B_k G^T s_0$ 
4:   for  $k = 0, \dots, K - 1$  do ▷  $K$  Iterations of Conjugate Gradient
5:      $p_k = -r_k + \beta_{k-1} p_{k-1}$ 
6:      $\alpha_k = \|r_k\|_2^2 / \|Gp_k\|_2^2$ 
7:      $m_{k+1} = m_k + \alpha p_k$ 
8:      $s_{k+1} = s_k + \alpha Gp_k$ 
9:      $r_{k+1} = B_k G^T s_{k+1}$ 
10:     $\beta = \|r_{k+1}\|_2^2 / \|r_k\|_2^2$ 
11:   end for
12:   return  $m_K$ 
13: end procedure
```

3. EXPERIMENTAL METHODS

Figure 3 shows the ground-truth sound speed map from a numerical breast phantom used to simulate pulse travel times from a surrounding ring of transducer elements. This sound speed map was adapted and modified from a contrast-enhanced cone-beam breast CT image in work from the Diagnostic Breast Center Göttingen (<https://doi.org/10.1016/j.tranon.2017.08.010>)²¹ under the Creative Commons Attribution-NonCommercial-No Derivatives License (CC BY NC ND) (<https://creativecommons.org/licenses/by-nc-nd/4.0/>).

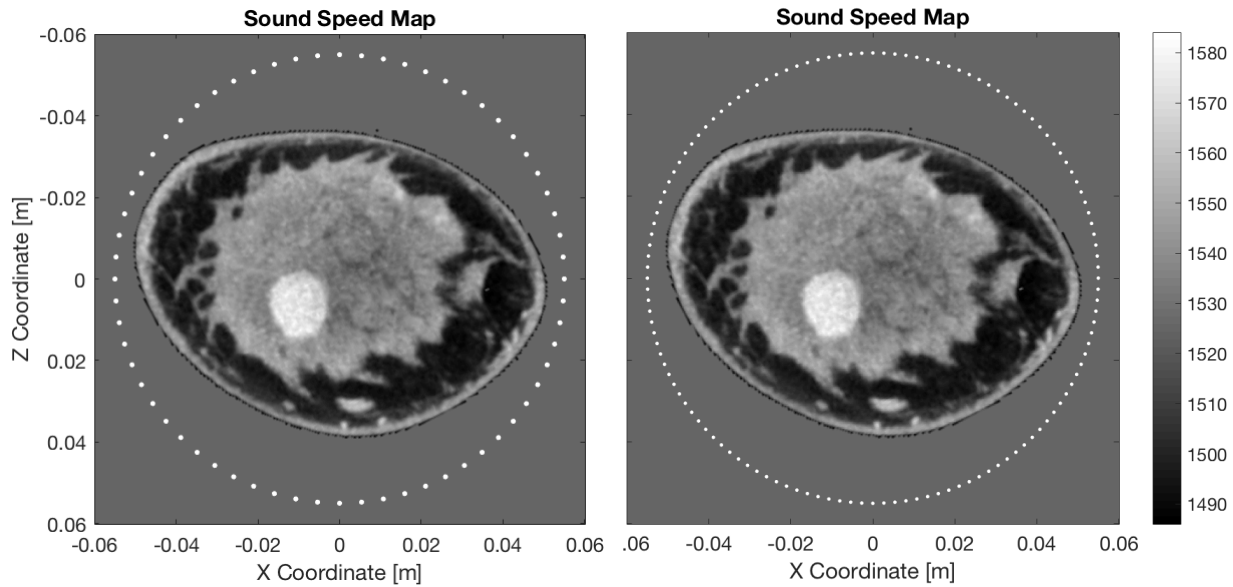


Figure 3. Same heterogeneous sound speed medium (Figure 1) surrounded by an $N = 64$ and $N = 128$ element array.

Each simulation has a ring array composed of $N_{elem} = 64$ or 128 elements. FMM is run once for each transmit element to obtain the travel times to each of the other N_{elem} receive elements on the array. These travel times make up a total of $m = N_{elem}^2$ entries in t_{obs} . Gaussian random noise with 10 ns standard deviation was added to the simulated travel times to emulate the errors due to travel time selection. These simulations do not include diffraction effects.

A separate simulation of the full wave equation was run using the k-Wave simulation package³⁰ with the numerical breast phantom and transducer ring setup shown in Figure 4. Travel times were selected according to the first-break method¹⁴ in order to avoid selecting times based on arrivals that are more energetic than the

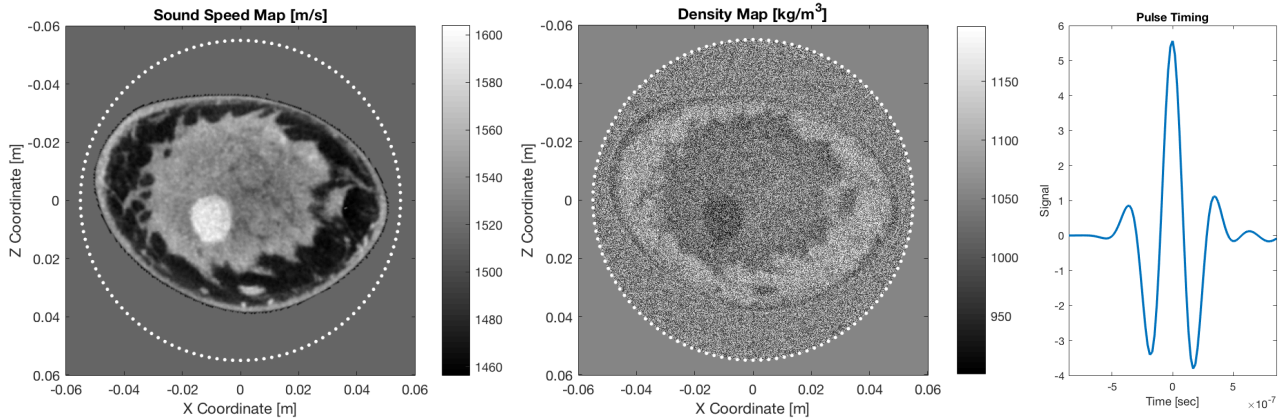


Figure 4. Sound Speed [m/s], Density [kg/m^3], 128-Element Transducer Ring, and 2.5 MHz Pulse in k-Wave Simulation

first wave arrival. It was essential to chose a method that was most sensitive to the first wave arrival because, although the eikonal equation is able to model all arrivals,³¹ FMM is only able to solve for the first arrival.

For each set of travel times (either simulated or estimated), each of the three reconstruction techniques (Laplacian regularized, Bayesian, and resolution-filling) were applied to reconstruct the sound speed distribution. Each sound speed reconstruction used $N = 4$ iterations of the Gauss-Newton method, each with $K = 500$ iterations of conjugate gradient. Reconstruction accuracy was then measured using root mean square (RMS) error in units of sound speed [m/s].

4. NUMERICAL RESULTS

Figures 5 and 6 show the first and last iterations of the Gauss-Newton method with FMM-simulated travel times from the 64 (Figure 5) and 128 (Figure 6) element ring arrays using Laplacian regularization, the Bayesian approach, and resolution-filling gradients. In each case, the first iteration of the Gauss-Newton method gives the sound speed reconstruction assuming straight ray paths. The distortions seen from the first iteration include expansion of high sound speed regions and shrinkage of low sound speed regions, which is mainly due to the fact that the true ray paths crowd around high sound speed regions (as seen in Figure 2) but reconstruction occurs on straight ray paths because of the initial uniform sound speed guess. However, with continued iterations of the Gauss-Newton method, the reconstructed sound speed is used to calculate the refracted ray paths over which the acoustic wave travels, further refining our sound speed estimates. In all cases, the RMS sound speed reconstruction error improves between the first and last iterations of the Gauss-Newton method. Regardless of the number of elements on the array, the final reconstruction avoids the geometric distortions seen after the first iteration of the Gauss-Newton method.

When only 64 elements (Figure 5) were used on the transducer ring, improvement in RMS error was smaller due to the decrease in resolution. The best improvement in RMS error was seen when using Laplacian regularization, followed by the resolution-filling gradient technique, and the Bayesian approach. One possible reason for this is that Laplacian regularization helps enforce continuity while minimally disturbing the reconstruction process. On the other hand, the Bayesian approach relies on the fixed covariance structure imposed by the Gaussian blurring operator Q , which limits the resolution of the final reconstruction. The improvement in RMS error as a result of using resolution-filling gradients comes close to that of Laplacian regularization because it balances blurring (from the Bayesian approach) with the goal of improving resolution. Decreasing the radius of the blurring kernel at each iteration allows improvements in resolution not previously achievable in the Bayesian approach. In this regard, Laplacian regularization and resolution-filling gradients work in opposite directions: Laplacian regularization tries to improve image smoothness whereas resolution-filling gradients try to resolve smaller structure with each iterations. When 128 elements (Figure 6) were used for imaging on the transducer ring, RMS error and resolution in the final reconstruction improved. In this case, reconstructions from using Laplacian regularization, the Bayesian approach, and resolution-filling gradients were very similar to each other.

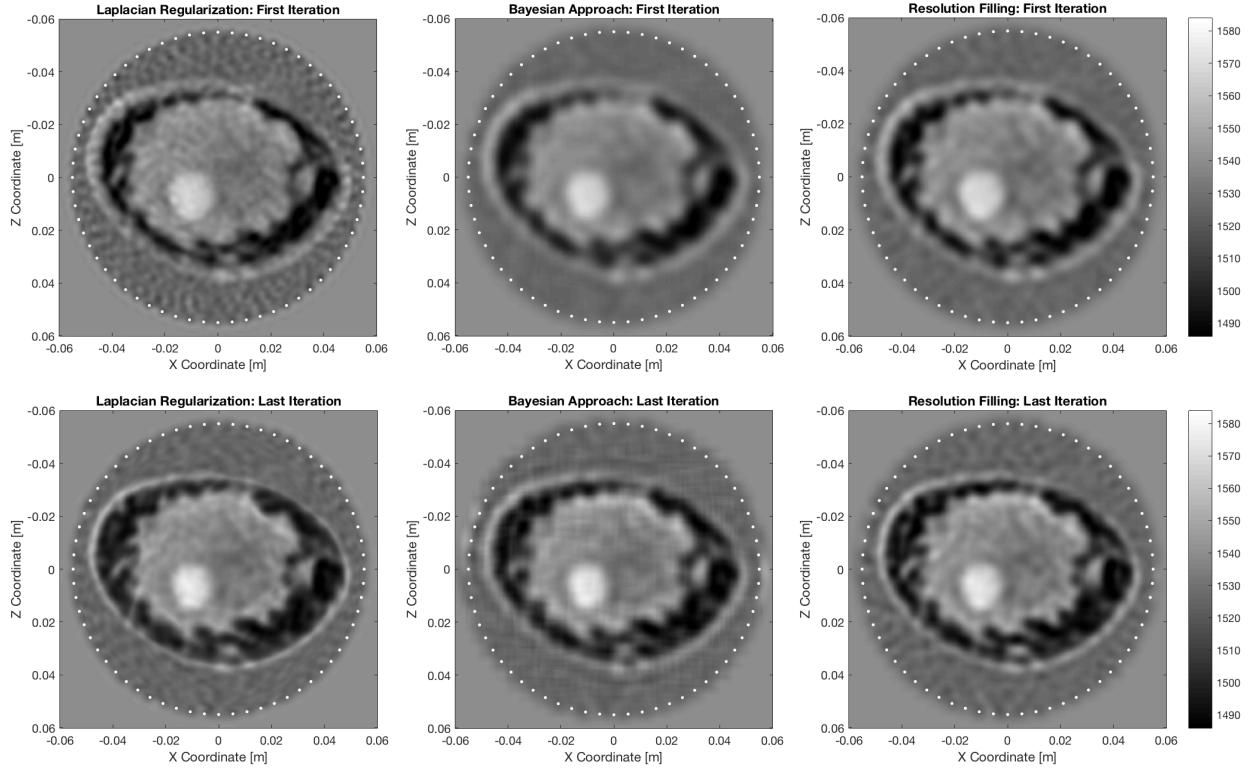


Figure 5. First and Last Iterations of the Gauss-Newton Method Using Laplacian Regularization, the Bayesian Framework, and Resolution-Filling Gradients using FMM-Simulated Travel Times with a 64-Element Ring. Between the first and last iterations of the Gauss-Newton method, RMS error in sound speed reconstruction improves from 8.4936 to 5.7199 m/s, 8.1644 to 6.6252 m/s, and 8.0096 to 5.9844 m/s, for each method respectively.

All results shown thus far use travel times directly simulated using FMM. However, these travel times generally have to be estimated from channel signals for each transmit and receive element pair. FMM calculates the branch of first arrival solutions to the eikonal equation, but the physics of diffraction can make it difficult to accurately measure these first-arrival travel times from time-domain signals. More energetic arrivals may follow the first arrival, and the amplitude of the first-arrival signal can vary across the array.

Although the main focus of this paper is to demonstrate a series of Gauss-Newton methods for recovering the sound speed distribution from first-arrival travel times, the difficulties of travel time selection and its consequences on sound speed reconstruction are also considered here. Figure 7 show the signals received by each element due to the transmission from the first element. Delaying signals based on the average background sound speed allows wavefronts to be visualized more clearly. Although the FMM solution accurately predicts the shape of the first-arrival wavefront simulated in k-Wave, the travel times measured using the first-break method do not perfectly agree with the FMM-predicted travel times. Although the first-break method avoids time selection based on arrivals more energetic than the first arrival, amplitude variation across the first-arrival wavefront can cause slight errors in measured first-arrival travel times. Repeating this process for each transmitting element yields a sinogram (Figure 8) for the travel time perturbation relative to the background sound speed of 1515 m/s.

Despite the overall agreement between sinograms based on FMM and the first-break method, errors between the two sinograms have a significant impact on the achievable quality of image reconstruction. The parameters of each reconstruction technique were adjusted to more strongly enforce spatial smoothness in the reconstruction so that stable convergence of the Gauss-Newton method could be achieved in the presence of errors in the first-break travel times. Spatial smoothness was enforced by increasing the α in Laplacian regularization and increasing the radius of the Gaussian blur in both the Bayesian and resolution-filling approaches.

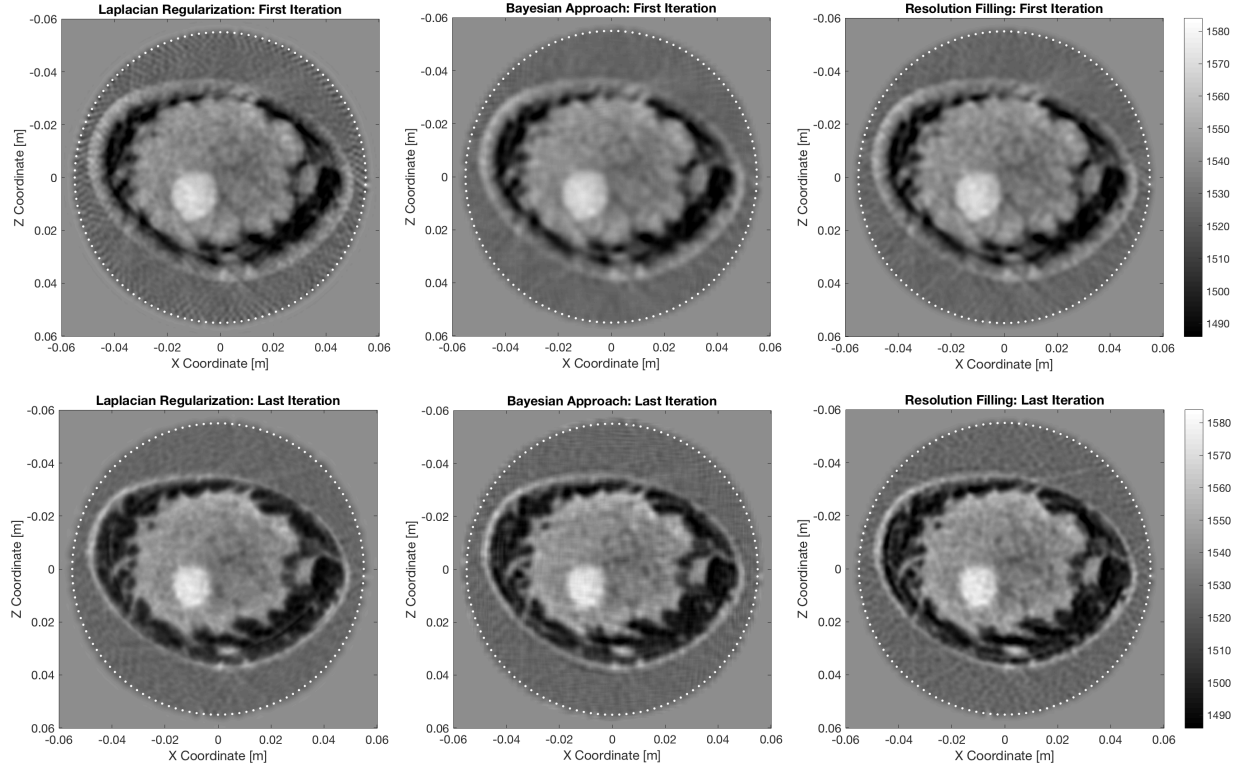


Figure 6. First and Last Iterations of the Gauss-Newton Method Using Laplacian Regularization, the Bayesian Framework, and Resolution-Filling Gradients using FMM-Simulated Travel Times with a 128-Element Ring. Between the first and last iterations of the Gauss-Newton method, RMS error in sound speed reconstruction improves from 8.3572 to 4.6097 m/s, 7.9964 to 4.7784 m/s, and 8.2195 to 4.8868 m/s, for each method respectively.

However, these adjustments also came at the cost of imaging resolution. Figure 9 shows this resolution loss across all reconstruction techniques. Again, the first iteration of the Gauss-Newton method shows the standard artifacts of ray-paths crowding around high sound speed regions as seen before in Figures 5 and 6. However, this artifact is no longer present in the final Gauss-Newton iteration for each reconstruction technique. RMS error in sound speed reconstruction reduces only by a small amount between the first and last iteration of the Gauss-Newton method, mainly because of the loss in resolution. Despite this loss in reconstruction quality and accuracy, the methods presented in this paper are applicable to travel times in which significant errors may be present. This requires adjustments to reconstruction parameters that promote the spatial smoothness of the reconstructed sound speed distribution.

5. DISCUSSION AND CONCLUSIONS

Ultimately, the goal of this paper is to summarize, implement, and demonstrate the Gauss-Newton method for refraction-corrected (or bent-ray) ultrasound computed tomography. We consider three main variations on the basic approach: Laplacian regularization, Bayesian framing, and resolution-filling gradients. All approaches have been shown to accurately reconstruct the sound speed distribution given knowledge of the first-arrival travel times. We provide open-source examples of each variation on the basic Gauss-Newton sound speed reconstruction technique, which is currently being maintained on Github: <https://github.com/rehmanali1994/refractionCorrectedUSCT.github.io>. These examples use FMM-simulated travel times to perform sound speed reconstruction.

However, in general, these first-arrival travel times need to be estimated from signals received by each element from a single-element transmission. The ability to accurately measure the first-arrival travel time from channel

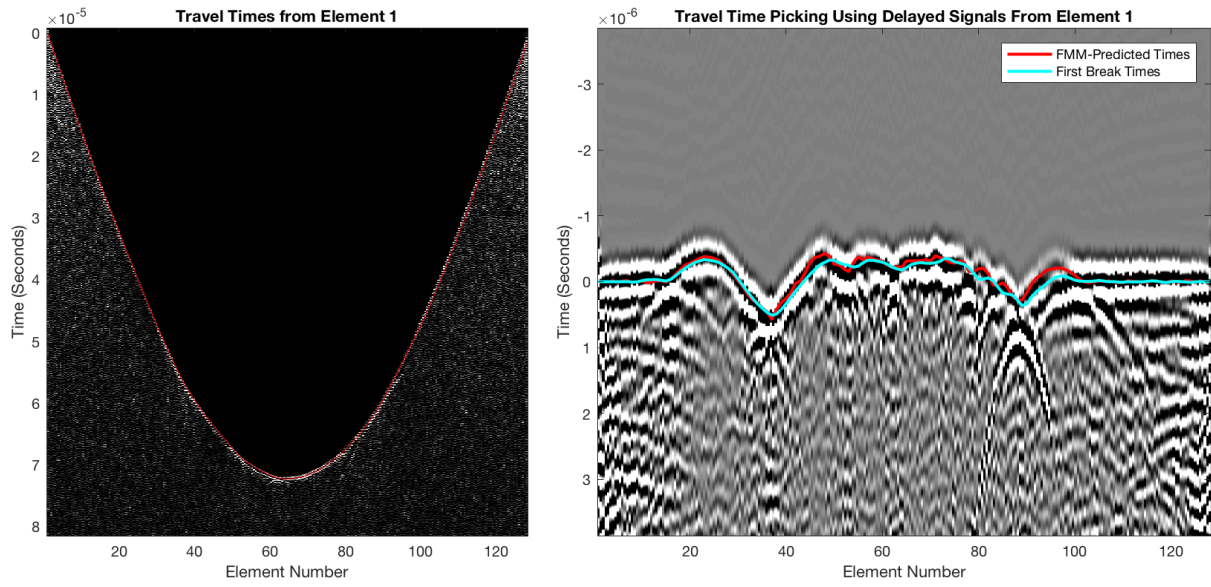


Figure 7. Channel Traces from k-Wave Simulation and Travel-Time Picking from the First Transmit Element. The raw signal traces from the k-Wave simulation were delayed according to the background sound speed (1515 m/s), leaving behind signals showing the higher-order travel-time perturbations due to the heterogeneity in sound speed. The first-break method was used to avoid picking travel times from more energetic arrivals

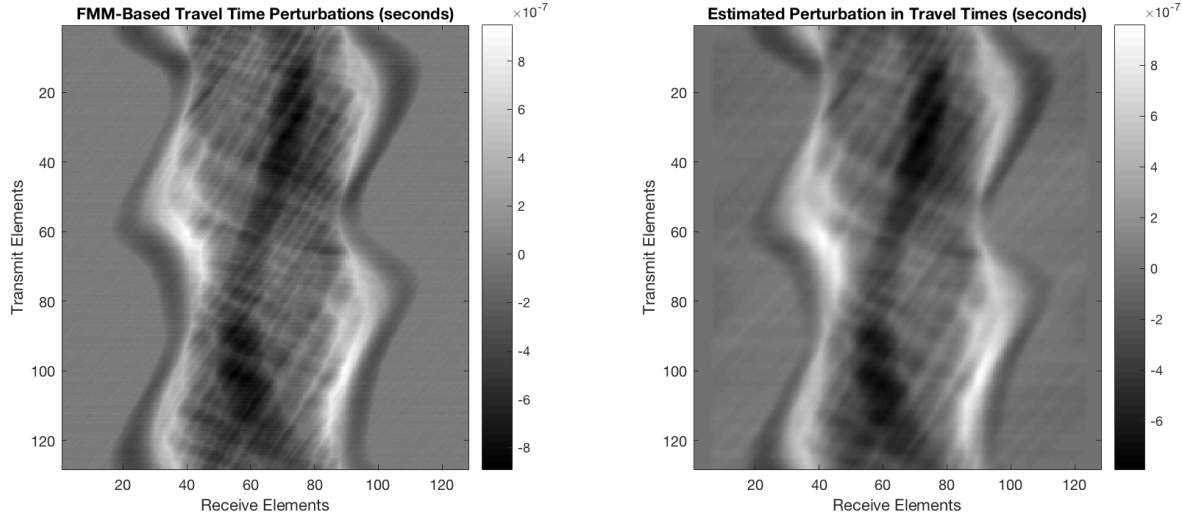


Figure 8. Travel Times Perturbations (relative to 1515 m/s) from Each Element on Transducer Ring Formatted as a Sinogram

data is ultimately limited by diffraction.³² This limitation has motivated further research on improved travel time selection.^{14,33–35} FWI can generally overcomes this limitation and produce highly spatially-resolved sound speed reconstructions.^{4,11,12} Some approaches interleave refraction correction techniques with FWI for further improvements in performance.³⁶

We applied the first-break method¹⁴ for travel time selection to signals (simulated in k-Wave) from each element on the array. Inaccuracy in the travel time selection method requires stronger enforcement of spatial

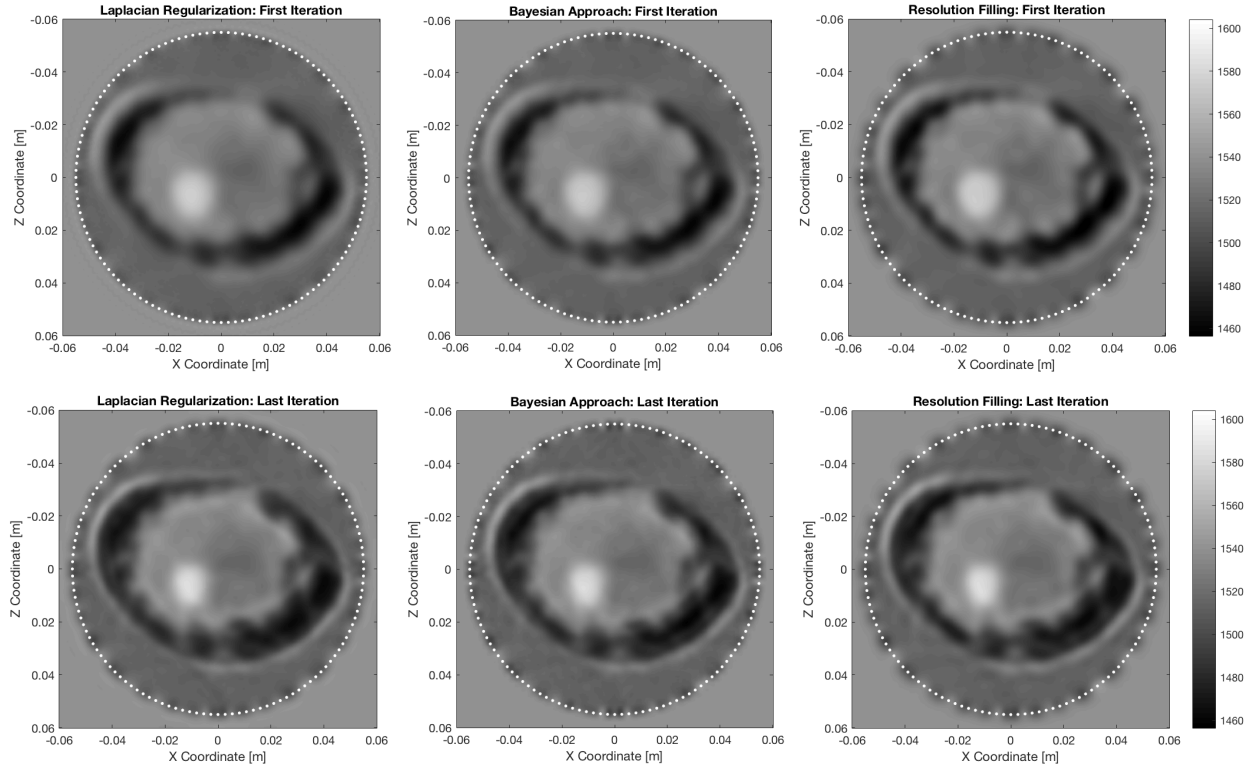


Figure 9. First and Last Iterations of the Gauss-Newton Method Using Laplacian Regularization, the Bayesian Framework, and Resolution-Filling Gradients using First-Break Travel Times from Simulated Data in k-Wave. Between the first and last iterations of the Gauss-Newton method, RMS error in sound speed reconstruction improves from 14.0511 to 12.8367 m/s, 14.1118 to 12.9204 m/s, and 13.9202 to 12.6564 m/s, for each method respectively.

smoothness in the reconstructed sound speed distribution. Although this comes at the cost of spatial resolution, the reconstruction techniques are still able to correct for refraction, which shows the applicability of the techniques in this work to travel time data. Resolution and reconstruction accuracy can be improved if better travel time selection techniques are employed.

ACKNOWLEDGMENTS

We would like to acknowledge Dr. Peter Kitanidis, from the Institute for Computational and Mathematical Engineering and the Civil and Environmental Engineering Department at Stanford University, for his expertise and advice on imaging inverse problems. We would also like to acknowledge Dr. John Pauly from the Department of Electrical Engineering at Stanford University for his expertise and advice on medical image reconstruction. We would like to further acknowledge feedback from various faculty within the Stanford Radiological Sciences Laboratory (RSL) such as Dr. Kim Pauly and Dr. Norbert Pelc. Finally, we would like to acknowledge the National Defense Science and Engineering Graduate (NDSEG) Fellowship for sponsoring Rehman Ali's graduate work.

REFERENCES

- [1] Li, C., Duric, N., Littrup, P., and Huang, L., "In-vivo breast sound-speed imaging with ultrasound tomography," *Ultrasound in Medicine and Biology* **35**(10), 1615–1628 (2009).
- [2] Duric, N., Littrup, P., Poulo, L., Babkin, A., Pevzner, R., Holsapple, E., Rama, O., and Glide, C., "Detection of breast cancer with ultrasound tomography: First results with the computed ultrasound risk evaluation (CURE) prototype," *Medical physics* **34**(2), 773–785 (2007).

- [3] Schreiman, J., Gisvold, J., Greenleaf, J. F., and Bahn, R., "Ultrasound transmission computed tomography of the breast," *Radiology* **150**(2), 523–530 (1984).
- [4] Wiskin, J., Borup, D., Johnson, S., and Berggren, M., "Non-linear inverse scattering: high resolution quantitative breast tissue tomography," *The Journal of the Acoustical Society of America* **131**(5), 3802–3813 (2012).
- [5] Kolb, T. M., Lichy, J., and Newhouse, J. H., "Occult cancer in women with dense breasts: detection with screening US—diagnostic yield and tumor characteristics," *Radiology* **207**(1), 191–199 (1998).
- [6] Kolb, T. M., Lichy, J., and Newhouse, J. H., "Comparison of the performance of screening mammography, physical examination, and breast US and evaluation of factors that influence them: an analysis of 27,825 patient evaluations," *Radiology* **225**(1), 165–175 (2002).
- [7] Ruiter, N. V., Göbel, G., Berger, L., Zapf, M., and Gemmeke, H., "Realization of an optimized 3D USCT," in [*Medical Imaging 2011: Ultrasonic Imaging, Tomography, and Therapy*], **7968**, 796805, International Society for Optics and Photonics (2011).
- [8] Carson, P. L., Meyer, C. R., Scherzinger, A. L., and Oughton, T. V., "Breast imaging in coronal planes with simultaneous pulse echo and transmission ultrasound," *Science* **214**(4525), 1141–1143 (1981).
- [9] Zalev, J., Herzog, D., Clingman, B., Miller, T., Kist, K., Dornbluth, N. C., McCorvey, B. M., Otto, P., Ermilov, S., Nadvoretsky, V., et al., "Clinical feasibility study of combined optoacoustic and ultrasonic imaging modality providing coregistered functional and anatomical maps of breast tumors," in [*Photons Plus Ultrasound: Imaging and Sensing 2012*], **8223**, 82230A, International Society for Optics and Photonics (2012).
- [10] Xia, J., Huang, C., Maslov, K., Anastasio, M. A., and Wang, L. V., "Enhancement of photoacoustic tomography by ultrasonic computed tomography based on optical excitation of elements of a full-ring transducer array," *Optics letters* **38**(16), 3140–3143 (2013).
- [11] Wang, K., Matthews, T., Anis, F., Li, C., Duric, N., and Anastasio, M. A., "Waveform inversion with source encoding for breast sound speed reconstruction in ultrasound computed tomography," *IEEE transactions on ultrasonics, ferroelectrics, and frequency control* **62**(3), 475–493 (2015).
- [12] Krebs, J. R., Anderson, J. E., Hinkley, D., Neelamani, R., Lee, S., Baumstein, A., and Lacasse, M.-D., "Fast full-wavefield seismic inversion using encoded sources," *Geophysics* **74**(6), WCC177–WCC188 (2009).
- [13] Hormati, A., Jovanović, I., Roy, O., and Vetterli, M., "Robust ultrasound travel-time tomography using the bent ray model," in [*Medical Imaging 2010: Ultrasonic Imaging, Tomography, and Therapy*], **7629**, 76290I, International Society for Optics and Photonics (2010).
- [14] Quan, Y. and Huang, L., "Sound-speed tomography using first-arrival transmission ultrasound for a ring array," in [*Medical Imaging 2007: Ultrasonic Imaging and Signal Processing*], **6513**, 651306, International Society for Optics and Photonics (2007).
- [15] Norton, S. J. and Linzer, M., "Correcting for ray refraction in velocity and attenuation tomography: a perturbation approach," *Ultrasonic imaging* **4**(3), 201–233 (1982).
- [16] Kalender, W. A., "X-ray computed tomography," *Physics in Medicine & Biology* **51**(13), R29 (2006).
- [17] Andersen, A. H. and Kak, A. C., "Simultaneous algebraic reconstruction technique (SART): a superior implementation of the ART algorithm," *Ultrasonic imaging* **6**(1), 81–94 (1984).
- [18] Jiang, M. and Wang, G., "Convergence of the simultaneous algebraic reconstruction technique (SART)," *IEEE Transactions on Image Processing* **12**(8), 957–961 (2003).
- [19] Sethian, J. A. and Popovici, A. M., "3-D traveltime computation using the fast marching method," *Geophysics* **64**(2), 516–523 (1999).
- [20] Sethian, J. A., [*Level set methods and fast marching methods: evolving interfaces in computational geometry, fluid mechanics, computer vision, and materials science*], vol. 3, Cambridge university press (1999).
- [21] Uhlig, J., Fischer, U., von Fintel, E., Stahnke, V., Perske, C., Lotz, J., and Wienbeck, S., "Contrast enhancement on cone-beam breast-ct for discrimination of breast cancer immunohistochemical subtypes," *Translational oncology* **10**(6), 904–910 (2017).
- [22] Aster, R. C., Borchers, B., and Thurber, C. H., [*Parameter estimation and inverse problems*], Elsevier (2018).
- [23] Nocedal, J. and Wright, S. J., "Conjugate gradient methods," *Numerical optimization* , 101–134 (2006).

- [24] Ruiter, N. V., Zapf, M., Hopp, T., Gemmeke, H., and van Dongen, K. W., "Usct data challenge," in [*Medical Imaging 2017: Ultrasonic Imaging and Tomography*], **10139**, 101391N, International Society for Optics and Photonics (2017).
- [25] Ruiter, N. V., Zapf, M., Hopp, T., Gemmeke, H., van Dongen, K. W., Camacho, J., Herraiz, J. L., Liva, M. P., and Udías, J. M., "Usct reference data base: conclusions from the first spie usct data challenge and future directions," in [*Medical Imaging 2018: Ultrasonic Imaging and Tomography*], **10580**, 10580Q, International Society for Optics and Photonics (2018).
- [26] Hassouna, M. S. and Farag, A. A., "Multistencils fast marching methods: A highly accurate solution to the eikonal equation on cartesian domains," *IEEE transactions on pattern analysis and machine intelligence* **29**(9) (2007).
- [27] Bærentzen, J. A., "On the implementation of fast marching methods for 3d lattices," (2001).
- [28] Kalman, R. E. et al., "A new approach to linear filtering and prediction problems [j]," *Journal of basic Engineering* **82**(1), 35–45 (1960).
- [29] Haykin, S., [*Kalman filtering and neural networks*], vol. 47, John Wiley & Sons (2004).
- [30] Treeby, B. E. and Cox, B. T., "k-wave: Matlab toolbox for the simulation and reconstruction of photoacoustic wave fields," *Journal of biomedical optics* **15**(2), 021314 (2010).
- [31] Fomel, S. and Sethian, J. A., "Fast-phase space computation of multiple arrivals," *Proceedings of the National Academy of Sciences* **99**(11), 7329–7334 (2002).
- [32] Li, C. and Duric, N., "Resolution limitation of travel time tomography: beyond the first fresnel zone," in [*Medical Imaging 2013: Ultrasonic Imaging, Tomography, and Therapy*], **8675**, 86751D, International Society for Optics and Photonics (2013).
- [33] Li, C., Huang, L., Duric, N., Zhang, H., and Rowe, C., "An improved automatic time-of-flight picker for medical ultrasound tomography," *Ultrasonics* **49**(1), 61–72 (2009).
- [34] Roy, O., Li, C., and Duric, N., "Travel time denoising in ultrasound tomography," in [*Medical Imaging 2012: Ultrasonic Imaging, Tomography, and Therapy*], **8320**, 832006, International Society for Optics and Photonics (2012).
- [35] Qu, X., Azuma, T., Imoto, H., Raufy, R., Lin, H., Nakamura, H., Tamano, S., Takagi, S., Umemura, S.-I., Sakuma, I., et al., "Novel automatic first-arrival picking method for ultrasound sound-speed tomography," *Japanese Journal of Applied Physics* **54**(7S1), 07HF10 (2015).
- [36] Huthwaite, P., Simonetti, F., and Duric, N., "Combining time of flight and diffraction tomography for high resolution breast imaging: initial invivo results (l)," *The Journal of the Acoustical Society of America* **132**(3), 1249–1252 (2012).